



Full length article

# Fabrication of Au network by low-degree solid state dewetting: Continuous plasmon resonance over visible to infrared region

Jiliang Liu<sup>a</sup>, Lingling Chu<sup>a</sup>, Zhao Yao<sup>b</sup>, Sui Mao<sup>a,\*</sup>, Zhijun Zhu<sup>a</sup>, Jihoon Lee<sup>c</sup>, Jixing Wang<sup>a</sup>, Laurence A. Belfiore<sup>d</sup>, Jianguo Tang<sup>a,\*</sup>

<sup>a</sup> Institute of Hybrid Materials, National Center of International Research for Hybrid Materials Technology, National Base of International Science & Technology Cooperation, College of Materials Science and Engineering, Qingdao University, Qingdao 266071, PR China

<sup>b</sup> College of Electronic information, Qingdao University, Qingdao 266071, PR China

<sup>c</sup> College of Electronics and Information, Kwangwoon University, Nowon-gu Seoul 01897, Republic of Korea

<sup>d</sup> Department of Chemical and Biological Engineering, Colorado State University, Fort Collins, Colorado 80523, USA

## ARTICLE INFO

### Article History:

Received 9 November 2019

Revised 7 February 2020

Accepted 19 February 2020

Available online 24 February 2020

### Keywords:

Gold

Network nanostructure

Solid state dewetting

Near infrared

Polychromatic plasmon

## ABSTRACT

Solid state dewetting (SSD) of thin-film can trigger morphology evolution from continuous film to isolated nanostructures over percolation threshold. However, the Au thin-film fabricated by low-degree SSD, namely Au network nanostructures, showed a wider plasmon absorption over visible and mid-infrared region as compared to the fully-developed nanoparticles. The optical properties of Au networks is systematically investigated by assistant of finite difference-time domain (FDTD) analysis in terms of E-field distribution and extinction efficiency. It is shown that the semi-manufactured irregular nanostructure possess strong plasmon resonance even at the wavelength up to 1900 nm. The monochromic plasmon responds of corresponding low-developed and high-developed samples are examined by surface enhanced Raman spectroscopy with 532 nm laser excitation. And for polychromic light, solar simulator was employed to evaluate the photocurrent performance of TiO<sub>x</sub> / Au network hybrid film. The results suggest the Au network have large potentials to be utilized under polychromic LSPR excitation scenes such as solar irradiation to improve the photoelectric properties.

© 2020 Acta Materialia Inc. Published by Elsevier Ltd. All rights reserved.

## 1. Introduction

Localized surface plasmon resonance (LSPR) of free electrons that triggered by incident electric-magnetic wave can induce significant near-field enhancement, specific light extinction and hot electron generation [1], therefore, have been widely studied and demonstrated in surface enhanced Raman spectroscopy [2,3], photoacoustic technology [4], photoelectric devices [5], imaging system [6], display technology [7] and other optoelectronic applications. Metallic nanostructures (MNSs) are the most common LSPR materials due to their high Quality factor that determined by the nature permittivity. Over 3-folder enhancement on electromagnetic field have been achieved within the nano-gap between dimer nano-islands [2,8], which pushed the Raman spectroscopy resolution approaching to single molecular level with the enhancement factor of 10<sup>14</sup>.

Among the various LSPR metals, Au can be one of the most used instances whose resonance wavelength can be modulated over VIS-NIR regions [1,4,5,9]. The tunable behavior that lies in LSPR

wavelength and intensity derives from the variation of quality factor since the permittivity of NSs are quite sensitive to their morphology [10]. Thereby, for the NSs possessing a specific shape, the LSPR absorption is usually shown as peaks at relatively settled positions. For example, Au spherical NPs show LSPR peaks between 500 and 700 nm and the peaks of Au rods are usually observed in NIR region (along longitudinal) [11–13]. By the various fabrication approaches, e.g. lithography [14], solid state dewetting (SSD), wet chemistry [12] and combined processing technology [15], Au NSs with uniform shape and size can be obtained with sharp characteristic peaks, exhibiting strengthful LSPR with the excitation of monochromatic light, such as light-emitting-diodes and lasers. Nevertheless, when application scene is established under polychromatic light excitation, e.g. solar irradiation and Xenon light, the light utilization for LSPR excitation can be limited due to the spectral mismatch [16] and lead to a low LSPR excitation efficiency. Therefore, exploration of LSPR materials possessing wide excitation band is significant for the numerous applications based on.

Thin-film SSD is a widely used bottom-up fabrication method for metallic nanostructures, in which the thin-film undergo void nucleation, film rupture, rim retraction and nanostructure formation [17,18], as seen in Fig. 1. As the process of nanostructure formation is

\* Correspondence authors.

E-mail addresses: [maosui001@qdu.edu.cn](mailto:maosui001@qdu.edu.cn), [maosui001@163.com](mailto:maosui001@163.com) (S. Mao), [jianguotangde@hotmail.com](mailto:jianguotangde@hotmail.com) (J. Tang).

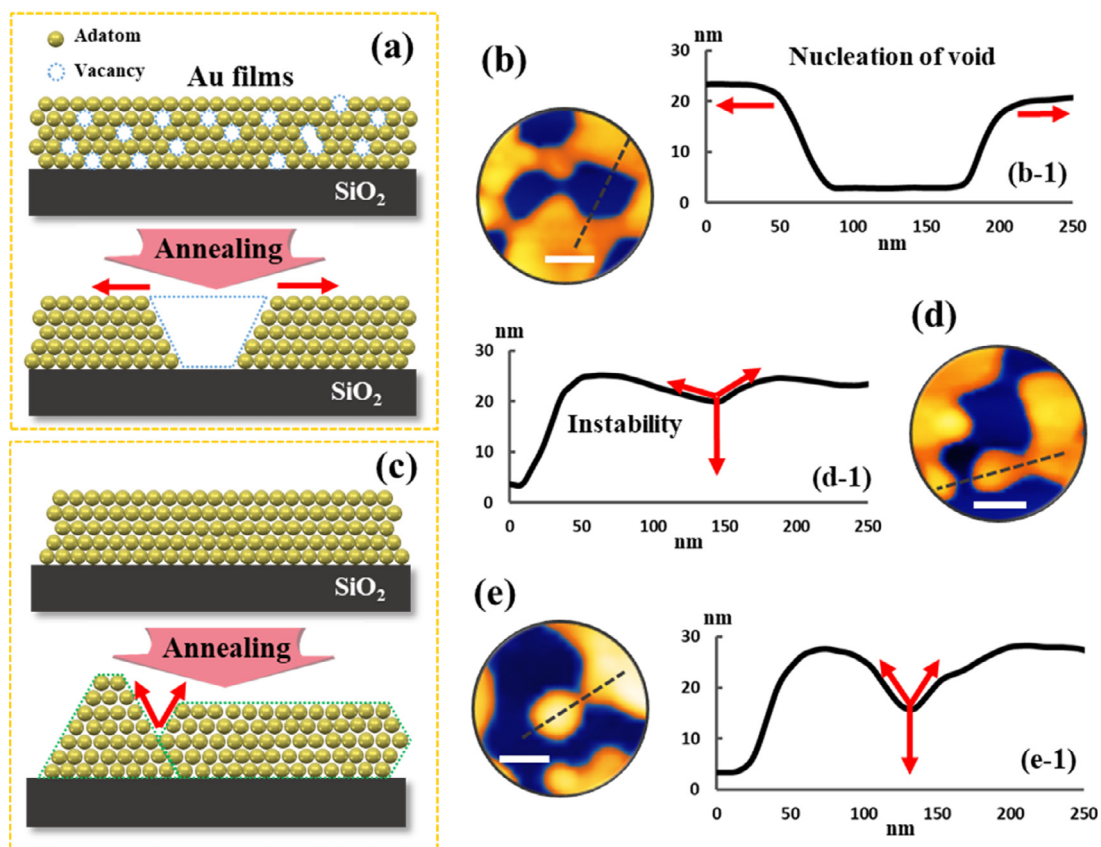


**Fig. 1.** Diagrams of Au film evolution through solid-state-dewetting. Cross-sectional schematic diagrams for (a) void nucleation and (c) instability. Nanostructure formation regimes of (b) void nucleation, (d) instability induced film fracture and (e) island isolation presented by atomic force microscopy (AFM) images and corresponding line-profiles.

relatively random, the low-developed nanostructures in early SSD stage can obtain wiggly shapes and thus lead to the various dielectric properties for individual nanostructures, which may give a new route for the research of wide-excitation LSPR material but rarely demonstrated yet. In current work, we demonstrate the fabrication of Au network NSs through low-degree SSD processing, in which an extremely wide LSPR absorption band was observed between 500 and 1900 nm. By the random formation behavior in SSD process, the mixture of Au NSs including hemispheres, rods and irregular NSs are formed with relatively stochastic configuration, therefore, each NS can exhibit dissimilar LSPR properties. The NS optical properties are systematically characterized and analyzed by the assistant of finite difference time domain (FDTD) simulation. Meanwhile, the monochromatic and polychromatic LSPR performance are separately evaluated by SERS and photon-detection.

## 2. Materials and methods

### 2.1. Nanoparticle (NP) fabrication

The various Au NPs were fabricated on double-side polished JGS1 quartz substrates that pre-treated by ultrasonic cleaning in acetone and ethanol for 10 min successively. The samples were dried by high pressure nitrogen flow before Au deposition. The Au films were deposited by direct current plasma sputtering with working gas (dry air) pressure of 6.5 Pa and a preset ionization current of 10 mA. The average Au deposition velocity is estimated as 0.03 nm/s. The film annealing was achieved inside an infrared furnace. The samples were heated to the target temperature with a ramping rate of 10 °C/s under the vacuum of ~10 Pa. After dwell duration, the samples were naturally cooled down inside the furnace chamber to 150 °C and then air-vented for further cooling until room temperature.

### 2.2. Surface enhanced Raman scattering

The Rhodamine 6 G (R6G, purchased from MACKLIN, 95%) was utilized as Raman reporters, and the R6G solution was prepared by dissolving in ethanol (AR, 98%). The R6G substrates were immersed into R6G solution ( $10^{-4}$  M) for 13 h to make sufficient molecular attachment. The confocal Raman microscope (inVia, Renishaw, UK) was employed for Raman spectra collection with a 532 nm excitation laser of 0.05 mW and a  $\times 50$  objective. The acquisition time was set as 5 s and accumulated for 30 cycles.

### 2.3. Fabrication of $\text{TiO}_x/\text{Au}$ hybrid film based photodetector

$\text{TiO}_x$  deposition was performed with sol-gel deposition of tetrabutyl titanate (purchased from Aladdin) as precursors. Tetrabutyl titanate solution was prepared by dissolving in dimethoxy ethanol (2-ME, from Aladdin). The Au/quartz samples were first coated with tetrabutyl titanate solution of 0.05 M and then spin at 3000 rpm for 20 s. Successively, the samples were annealed at 200 °C on hot-pad for 5 min to fully evaporate the 2-ME and also promote the hydrolysis of tetrabutyl titanate into  $\text{TiO}_x$ . After 10-time spin coating, the  $\text{TiO}_x/\text{Au}$ /quartz samples were placed into tube furnace to receive a 3 h annealing at 550 °C under atmosphere to improve the crystallinity. The Al electrodes were deposited by mask sputtering and the thickness of Al electrodes were ~50 nm.

### 2.4. Finite-difference time-domain (FDTD) simulation

The spectra and electro-magnetic field distribution of modeling structure were obtained through FDTD simulation (FDTD solutions, Lumerical, Canada). Total-field scattered-field (TFSF) light source was engaged with the injection axis of z to evaluate the absorption and

scattering properties of each modeled NS. Perfect matched layer (PML) boundary conditions were set for x-, y- and z-axis along with the mesh size 0.5 nm, and the simulation duration was set as 1000 fs with auto shutoff level of 1E-6. The permittivity values of Au refer to the Lermarchand based on their experimental data of an 11.7 nm-thick Au film [19], and the data of TiO<sub>x</sub> and quartz were from Sarkar [20] and Philipp [21], respectively. The error source analysis in simulation can be referred in supplementary Fig. S1 and S2.

2.5. Characterization

An atomic force microscopy (AFM, Molecular Vista, USA) was employed for morphological characterization under tapping mode and the probes employed in this work were PPP-NCHR (Nanosensors™, USA) with a typical tip height and radius of 17 μm and ~7 nm, respectively. The RMS, surface coverage, SAR and projected area were obtained by Gwyddion (open-source). The UV–VIS-IR optical characterization were achieved by an micro-spectrophotometer (20 PV, CRAIC Technologies, USA), in which the micro area of ~16 μm<sup>2</sup> was characterized through a × 36 objective with an objective-sample distance of ~10 mm. The cross-sectional SEM imaging were done via Schottky field emission SEM (JSM-7800F, JEOL, Japan) and the photocurrent characterization was obtained by a source-meter (Keithley 2400, Tektronix, USA). The simulation of solar irradiation was achieved by Xenon lamp simulator (7IS0503A, SOFN

instruments CO., LTD, China) with a working distance of 12 cm and an illumination power of 100 mW cm<sup>-2</sup>.

3. Result and discussion

3.1. Morphological and optical evolution

Fig. 1 shows the diagram of Au nanostructure formation in solid-state dewetting (SSD) process and Fig. 2 exhibits the evolution of Au NSs fabricated at 600 °C by the variation of annealing duration between 15 and 900 s. Generally, surface morphology of thin-film in SSD process can be largely determined by the Adatom immigration through thermal-activated surface diffusion [22,23]. Initialized from film defects such as pinholes, voids, gas bubbles or grain boundary triple points, heterogeneous nucleation of vacancies can occur in solid metallic film as shown in Fig. 1(a) and (b) [17,24]. Following the void growth and coalescence, continuous film can be penetrated and isolated into nanostructures with longer annealing duration, and eventually evolved by rim retraction into droplets via surface energy minimization induced instability as shown in Fig. 1(c)–(e) [25]. In specific, with 15 s annealing, voids were formed through heterogeneous nucleation and partially coalesced with each other as seen in Fig. 2(a). As a consequence, the continuous film evolved into overall networks as most of the NSs are still in connection. Soon after, when the annealing lasted to 300 s, the network was further separated by

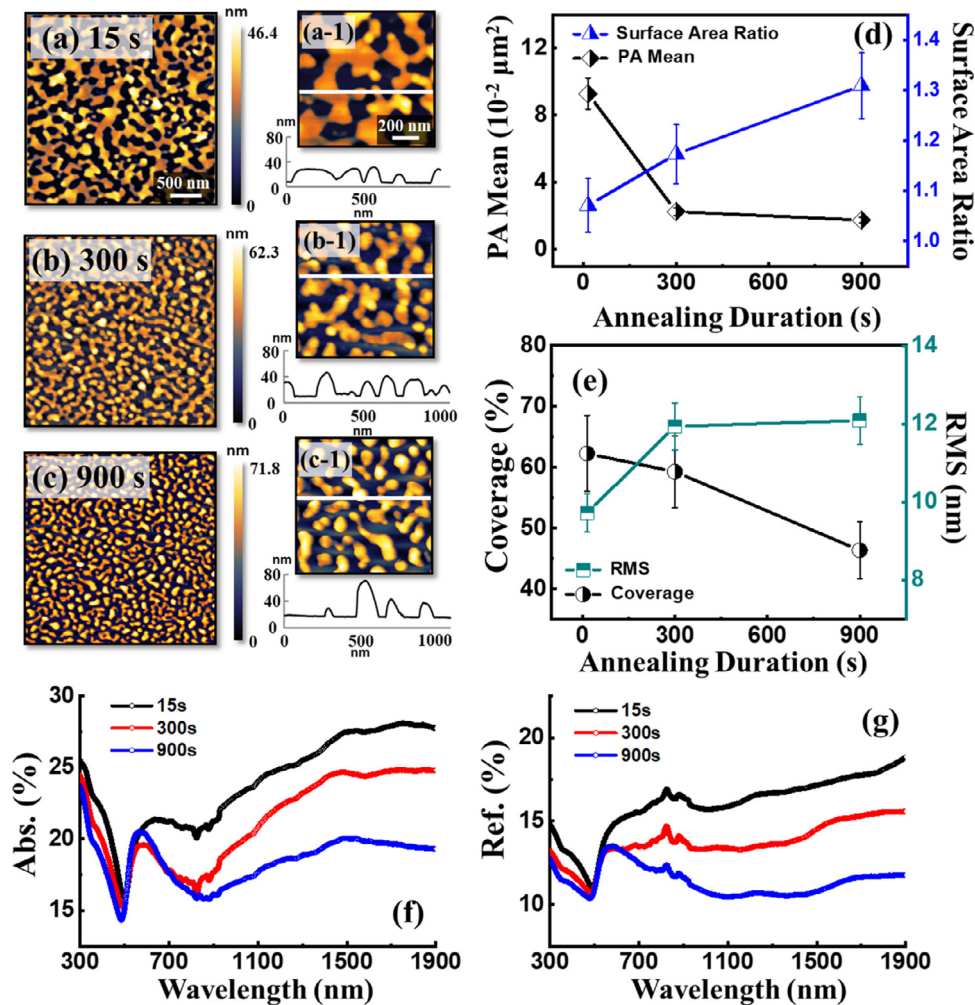
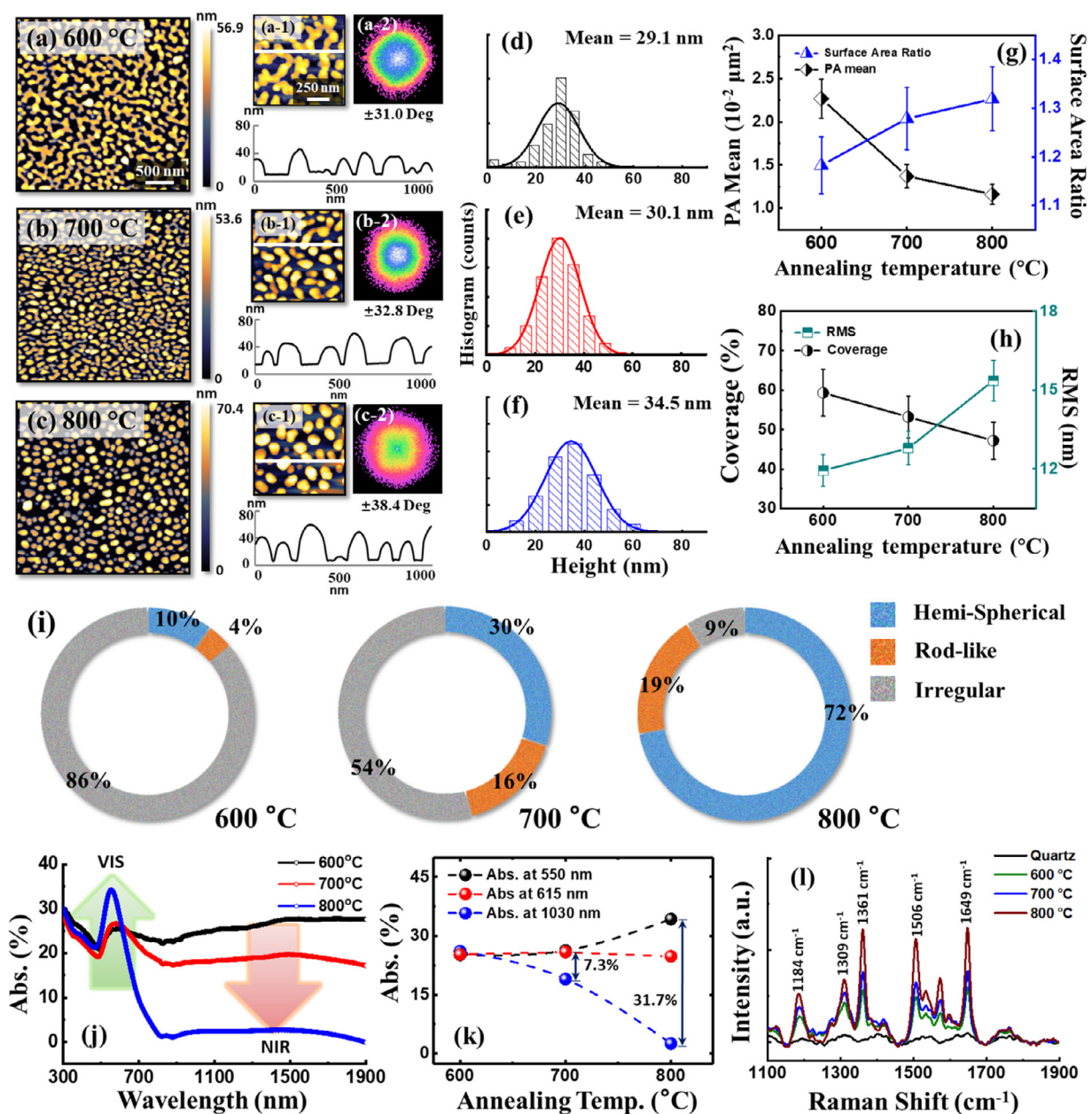


Fig. 2. Morphological and optical evolution of Au film annealed at 600 °C by the increasing time of (a) 15, (b) 300 and (c) 900 s. Plots of (d) nanostructure projected area (PA) mean on x-y plane, surface area ratio, (e) coverage and roughness along annealing time. (f) Absorption and (g) reflectance spectra for corresponding samples. Error range: ±5% for surface area ratio and RMS, ±10% for PA mean and coverage.

coalesced voids and evolved into more isolated NSs as exhibited by AFM images in Fig. 2(b). With longer annealing of 900 s, the wiggly NSs were further split into the NSs containing less surface energy, e. g. hemispherical nanoparticles (HS-NPs). Consequently, the NSs were formed in smaller but compacter configuration, seen in Fig. 2(c). The dimensional evolution can be observed via the projected area (PA) and surface area ratio (SAR) variation plotted in Fig. 2(d). At 15 s, the PA mean of NSs appeared  $9.3 \times 10^{-2} \mu\text{m}^2$  as the majority of nanostructures are connected in the networks. Then, at 300 s, most of the NSs were separated and the mean was sharply decreased to  $2.3 \times 10^{-2} \mu\text{m}^2$  as the nanostructures are separated by rim retraction. Lastly, the PA mean was further decreased to  $1.8 \times 10^{-2} \mu\text{m}^2$  with the NS separation. Meanwhile, from the SAR data, it is clear that the nanostructures were turned into compacter shape as the SAR was

increased from 1.07 to 1.17, and finally reached 1.31 at 900 s, matching with the inference by surface energy minimization mechanism. Moreover, RMS roughness of sample surface was correspondingly increased from 9.72 to 12.09 nm along with the configurational evolution as seen in Fig. 2(e). It is notable that the RMS evolution matched well with the evolution with PA mean, which indicate that RMS contribution from nanostructure separation can be larger than that from single nanostructure constriction (The relationship between effective thickness and RMS is plotted in supplementary Fig. S3). And at the same, the NS coverage showed a continuous decrease from ~62.3 to 46.4%.

Accompanying with the NS isolation, the continuous Au film passed through percolation threshold, therefore, triggered the transformation of overall electric susceptibility from metallic to dielectric



**Fig. 3.** Morphological evolution of Au nanostructures annealed at increasing temperature of (a) 600, (b) 700 and (c) 800 °C. (a) – (c) AFM images of  $3 \times 3 \mu\text{m}^2$ . (a-1) – (c-1) Enlarged AFM images of  $1 \times 1 \mu\text{m}^2$  and the line-profiles of locations indicated by white lines are shown below. (a-2) – (c-2) Slope distribution of nanostructures on x-y plane. (d) – (f) Histograms of nanostructure height. Plots of (g) projected area (PA) mean, surface area ratio, (h) coverage and RMS versus annealing temperature. (i) Pie chart summary of nanostructure components. (j) Absorption spectra of corresponding samples. (k) Evolution of absorption intensity at typical wavelength of VIS (550 and 615 nm) and NIR (1030 nm). (l) Raman spectra of Rhodamine-6 G using various Au nanostructures as SERS substrates. Error range:  $\pm 5\%$  for surface area ratio and RMS,  $\pm 10\%$  for PA mean and coverage.

[26,27]. As a consequence, the optical properties of Au films were correspondingly modified along with surface morphology, in which the resonance path of free electrons was confined locally when plasmon was activated. Evidenced by the absorption spectra in Fig. 2(f), the LSPR absorption peak in VIS region was gradually strengthened as more NSs were isolated, while the absorption in NIR region was correspondingly weakened oppositely. Consistently, from the reflectance spectra, it can be also seen that the VIS responds was enhanced while NIR reflection was much reduced.

As lifted temperature can enhance the surface diffusion of adatoms, the evolution from Au network to NPs was also achieved via temperature control. With the temperature modulated surface diffusion length [28–30], the overall SSD progress was significantly accelerated and led to a corresponding morphological evolution, exhibited in Fig. 3(a)–(c). Lifted temperature could be helpful to improve the large-scale uniformity, in which the void nucleation can happen more quickly and synchronously, therefore avoid the occurrence of localized morphology [24,29]. The height mean of NSs was gradually enlarged from 29.1 to 34.5 nm along with the temperature increase as seen in Fig. 3(d)–(f). At the same time, judged by the PA mean plotted in Fig. 3(g), the NSs were gradually retracted into smaller and compacter configuration as the average area was decreased from 2.3 to  $1.2 \times 10^{-2} \mu\text{m}^2$ . As compared with time-induced evolution, the temperature induced PA variation evolution is milder, which is also verified in SAR variation from 1.18 to 1.32. At the same time, the coverage was decrease from 60% to 47%. And for the RMS, the value was 11.94 nm for 600 °C, which was then increased to 12.8 nm at 700 °C and finally reached 15.4 nm at 800 °C. Again, it can be seen that the RMS evolution matched well with the variation of PA mean, which cross-verified that the instability induced nanostructure break can be main inducement for RMS increase (Analysis shown in supplementary Fig. S3). Furthermore, to evaluate the facet properties of NSs, the 2-D slope distribution of corresponding samples are shown in Fig. 3(a-2)–(c-2) and NSs were observed with no specific facial preference by round patterns. However, the flat top of NSs could be clearly observed as the low-degree part (blue) occupied a large area at pattern center for 600 °C sample. And at higher temperature, the flat-top of NSs gradually disappeared as the surface reconstruction was triggered by surface energy minimization when sufficient energy was supplied [31]. The componential evolution of NS, including HS-NP, rod and irregular NS, is summarized using pie charts in Fig. 3(c) by component ratios in order to make the morphology evolution more intuitive. As discribed previously, with the splitting of irregular NSs from 600 to 800 °C, the ratio of HS-NPs was increased from 10% to 72% while the irregular NSs were decreased from 86% to 9%. The evolution from continuous film to wiggly and hemi-spherical nanostructures was also observed by using other energy supply method such as pulse laser, so that the high-temperature process can be avoid from possible damage to the substrate with low thermal tolerance [32].

In terms of optical properties, similar evolution trend was observed owing to the morphological variation. Generally, the absorption in VIS region was continuously enhanced along with the formation of more isolated NSs while the absorption in NIR showed a decaying trend as seen in Fig. 3(k) (The corresponding reflectance spectra are shown in supplementary Fig. S4). Specifically, take 550 and 1030 nm as typical wavelength for VIS and NIR, the absorption at 550 nm was gradually increased from 25.2 to 34.3%, while the absorption at 1030 nm was decreased from 26.1 to 2.6%. As a consequence, with morphological evolution from 600 to 800 °C, the nearly equivalent absorption intensity in VIS and NIR was varied with a growing difference until 31.7%. The spectra indicate the great potentials of Au network to be utilized as a LSPR material for dual VIS-NIR region. To further varyify the plasmon properties of corresponding samples in VIS region, rhodamine-6 G (R6G) molecules were utilized as Raman reporters and the various samples were employed as SERS substrates to evaluate the LSPR effect on Raman signals excited by

532 nm laser. As displayed in Fig. 3(l), the characteristic peaks of R6G were not shown clearly on original quartz substrate owing to the ultra low molecular concentration of  $10^{-4}$  mol/L. However, by LSPR excitation, the nearfield intensity can be strengthened and assitant to magnify the Raman signal by 6 to 9 orders [33] as the enhancement factor is approximately proportional to  $|E|^4$  [34,35]. In contrast with quartz substrate, the Raman signals were clearly observed with all other Au NS substrates. According to the SERS signal intensity, the enhancement order was observed as  $800 > 700 > 600$  °C which is identical to the absorption intensity order at 532 nm as seen in Fig. 3(j). The SERS result indicates that the SERS enhancement matches with the strength of light-matter interaction (absorption), thus it can be concluded that the LSPR intensity of further developed NSs can be stronger in VIS region.

### 3.2. FDTD analysis for relationship between NSs and optical responsds

To futher explore the relationship between NSs and their optical properties, rigorous examination was performed by FDTD simulation for various NSs. The corresponding analysis was based on 5 individual NSs including the HS-NP, rod and 3 individual irregular NSs. The modeling and E-field distribution of HS-NPs and rods are shown in Fig. 4(a)–(d). The extinction cross-section  $\sigma_{\text{Ext}}$  of a NS that describes the scattering rate of unit incident light and the  $\sigma_{\text{Ext}}$  of specific wavelength  $\sigma_{\text{Ext}}(\lambda)$  can be expressed as  $\sigma_{\text{Ext}}(\lambda) = \text{Power}_{\text{total extinction}}(\lambda) / \text{Power}_{\text{source}}(\lambda)$ . At the same time, the dimensionless efficiency of light extinction at

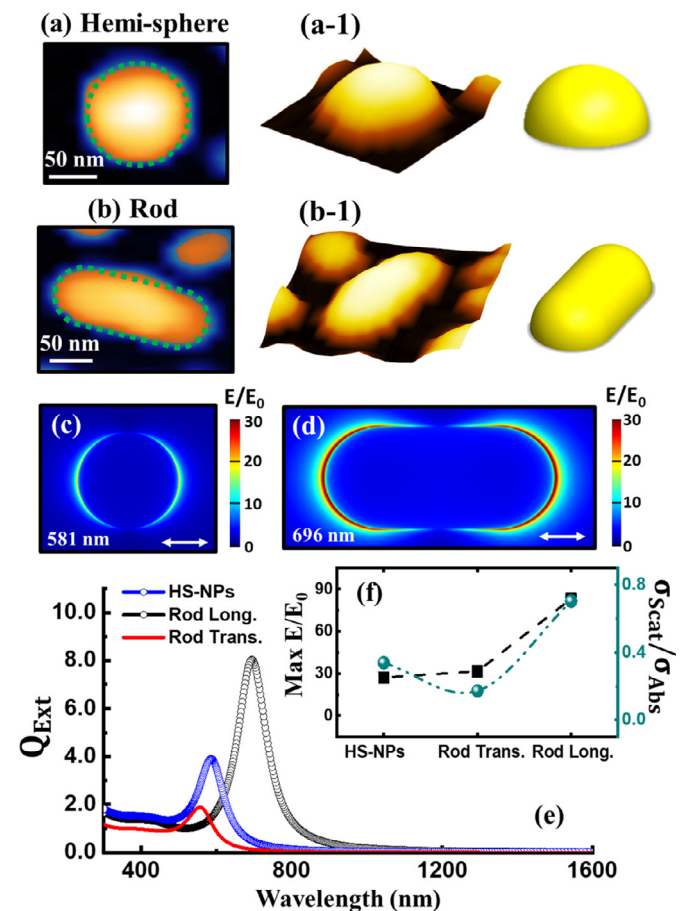


**Fig. 4.** Optical analysis in terms of E-field distribution and extinction efficiency by FDTD methods for the (a) hemi-sphere and (b) rod. (a-1) – (b-1) AFM 3-D views. (c) – (d) Corresponding E-field distribution with longitudinally polarized excitation. (e) Extinction efficiency for the hemi-sphere and rod along longitudinal and transverse directions, and (f) summary of maximum  $E/E_0$  values and scattering/absorption ratio.

specific wavelength  $Q_{Ext}(\lambda)$  is obtained by  $Q_{Ext}(\lambda) = \sigma_{Ext}(\lambda)/\sigma_{Geometric}$  and plotted in Fig. 4(e).

For the HS-NP, clear dipolar resonance was observed and the strongest excitation appeared at 581.7 nm with an  $\sigma_{Ext}$  of 6290 nm<sup>2</sup> and  $Q_{Ext}$  of 3.9. (The corresponding  $\sigma_{Ext}$  and geometric area was plotted in supplementary Fig. S5) Meanwhile, the maximum E-field intensity was enhanced by 27.2 times and the E/E<sub>0</sub> values were plotted in Fig. 4(g). For rod, the FDTD simulation was performed with the excitations along both transverse and longitudinal directions, as the difference in oscillation distance can significantly vary the LSPR wavelength. Consequently, the resonance wavelength 556 and 693 nm were respectively observed with the  $Q_{Ext}$  of 1.89 and 8.04 along transverse and longitudinal directions. And the maximum E-field intensity were observed as 31.6 and 83.2. Furthermore, the responding scattering and absorption cross-section  $\sigma_{Abs}$  and  $\sigma_{Scat}$  were calculated and the  $\sigma_{Scat}/\sigma_{Abs}$  ratio was plotted in Fig. 4(f) (Original spectra can be seen in Supplementary Fig. S6). In HS-NP case, the  $\sigma_{Scat}/\sigma_{Abs}$  ratio was calculated as 0.34, which indicates a relatively small component of scattering to extinction. However, the scattering was varied for rod, according to the excitation directions. As seen, the scattering was significantly increased to 0.70 in longitude direction, while smaller in transverse direction as 0.17. The scattering intensity can be largely determined by the resonance distance in light polarization direction [36], thus lead to a dimension and direction dependent behavior.

Fig. 5 shows the FDTD analysis for three irregular NSs, namely A, B and C. The 3 typical NSs were picked from AFM images and modelled by combining HS-NPs and rods as elements, in which the components are overlapped with each other to simulate the low-degree SSD state before totally isolated. (The morphology modelling details are shown in supplementary Fig. S2). In general, as compared with HS-NPs and rods, the irregular NSs showed higher E-field enhancement and extinction properties in NIR region especially along longitudinal excitation. Specifically, displayed by Fig. 5(a-2)–(c-2), the irregular NSs were excited in a dipolar resonance mode and the maximum E-field intensity is 106.4, 69.6 and 86.2 for model A, B and C as plotted in Fig. 5(e). And for extinction, in model A case, maximum extinction efficiency was observed at 1126.4 nm and 882.6 nm for longitudinal and transverse directions, respectively. And for B and C, the maximum extinction cross-section along longitudinal directions were observed at 1176 and 1807 nm with relatively weaker transverse extinction. And in terms of  $Q_{Ext}$ , model A, B and C all showed much enhanced extinction efficiency as witnessed in Fig. 5(d), reached even 10, exhibiting the strong capacity of light control. Furthermore, the  $\sigma_{Scat}/\sigma_{Abs}$  ratios of A, B and C in longitude direction were calculated and plotted in Fig. 5(e). As the volume of irregular NSs are larger as compared with single HS-NP or rod, the scattering components are significantly increased. Based on the values of  $\sigma_{Scat}/\sigma_{Abs}$  ratios, the scattering and absorption can be nearly equal with each other as seen in Fig. 5(e).

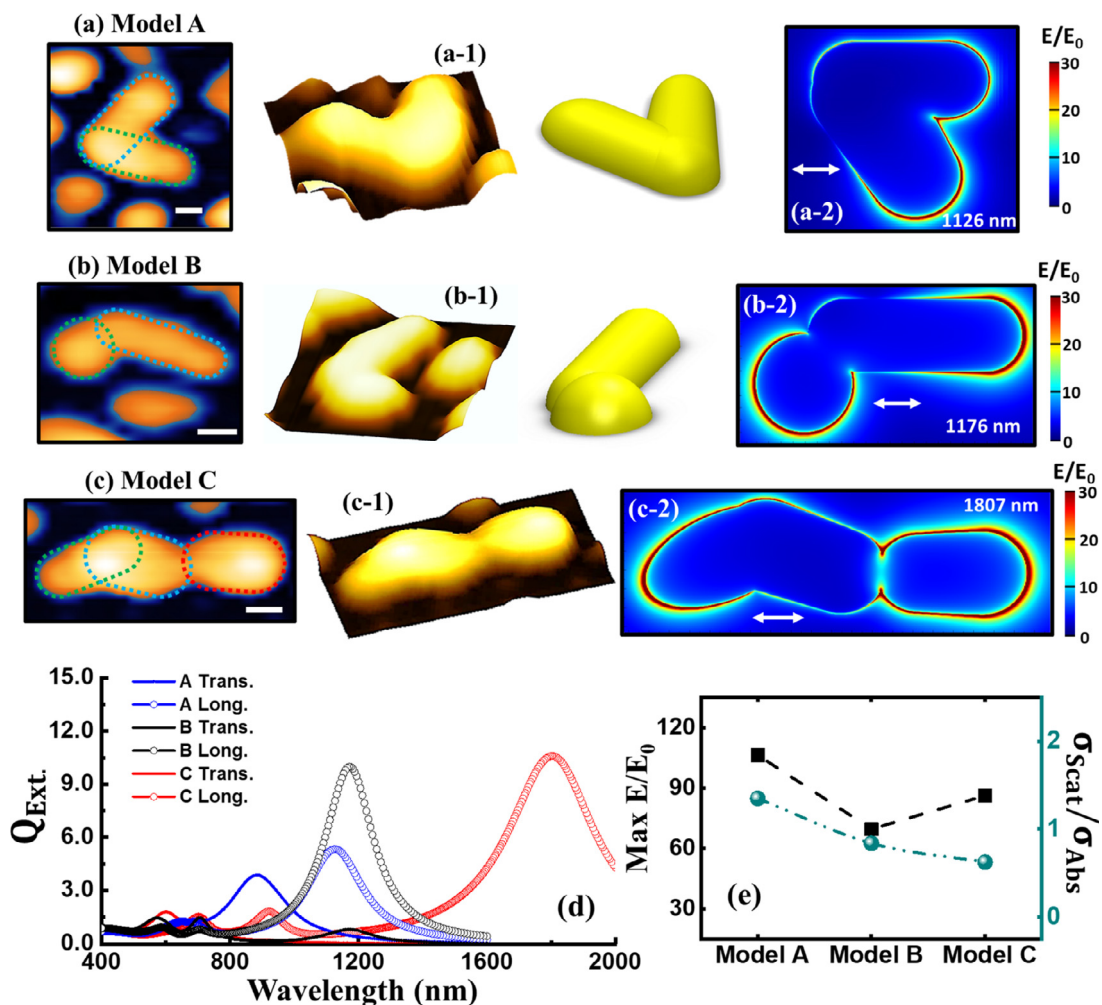


Fig. 5. Optical analysis via FDTD method for irregular nanostructures: (a) A (overlapped rods), (b) B (Hemisphere and rod) and (c) C (multiple rods). (a-1)–(c-1) AFM 3-D views for corresponding samples. (a-2)–(c-2) E-field distribution with longitudinally polarized excitation. (d) Extinction efficiency of A, B and C along transverse and longitudinal directions, and (e) summary of maximum E/E<sub>0</sub> values and scattering/absorption ratio.

Evidenced by the extinction cross-section, it can be concluded that, each individual NS with irregular shape usually possess characteristic excitation peaks in VIS-NIR region. As their configuration can be relatively random during the formation process via SSD, a continuous NIR LSPR absorption can be resulted with the overall surface morphology in a macro perspective. According to the observation in Fig. 3 (i), the absorption was last smoothly even beyond 1800 nm, which endows the surface a widespread plasmon responding region. Moreover, the E-field intensity was quite much enhanced even over 100, therefore, suggests that the NSs could be utilized for the purpose of NIR and even SWIR (short-wavelength IR, 1.4–3 μm) LSPR for the widespread of applications.

### 3.3. Dielectric effect of TiO<sub>x</sub> top-layer on Au LSPR

To explore the dielectric effect on Au network LSPR, TiO<sub>x</sub> thin films were deposited on top of Au networks via sol-gel approach to fabricate TiO<sub>x</sub>/Au hybrid films. The optical properties of TiO<sub>x</sub>/Au hybrid films were evaluated through gradually thickened TiO<sub>x</sub> top-layers as shown in Fig. 6(a), in which precursor solution of TiO<sub>x</sub> was spin-coated repeatedly by 10 times to generate the gradually increased dielectric environment. The Au network film after 10-time TiO<sub>x</sub> coating was observed as ~30 nm in thick as evidenced by the cross-sectional SEM in Fig. 6(b). The spectral evolution and related

analysis for the fabricated hybrid films are shown in Fig. 6(c)–(f). As seen in Fig. 6(d), pure TiO<sub>x</sub> displays the single peak in UV region (Reflectance spectra of pure TiO<sub>x</sub> are shown in supplementary Fig. S7), while obvious dual extinction was observed in UV and VIS-NIR regions with the Au NSs beneath. Meanwhile, in return, the dielectric effect from TiO<sub>x</sub> was also observed on Au absorption, in specific, the absorption peak of Au NSs was gradually red-shifted and the peak intensity was simultaneously enhanced as summarized in Fig. 6(e).

In general, contacting with high dielectric material can result in significant amplification to LSPR intensity for metallic NSs [9,37]. The extra dielectric top-layers can play roles as screenings and partially neutralize the charge density at NS surface, therefore, make the plasmon excitation at lower energy level. At the same time, the absorption was correspondingly increased as the extinction efficiency  $Q_{ext}$  can be enlarged with the surrounding media of larger refractive index [9,38]. As a result, the overall extinction intensity was enhanced from 12.9 to 35.4% and the peak position was redshifted from 566.3 to 582.9 nm along with the TiO<sub>x</sub> thickness increase. Through the post annealing of 550 °C, the absorption of hybrid film was further enhanced to 42.7% and the peak was simultaneously redshifted to 643.1 nm. The post annealing may decrease the defects also improve the crystallinity of TiO<sub>x</sub>, so that the dielectric effect can be correspondingly improved. The reflectance spectra also showed a similar evolution trend, while the reflectance peak is slightly redshifted in

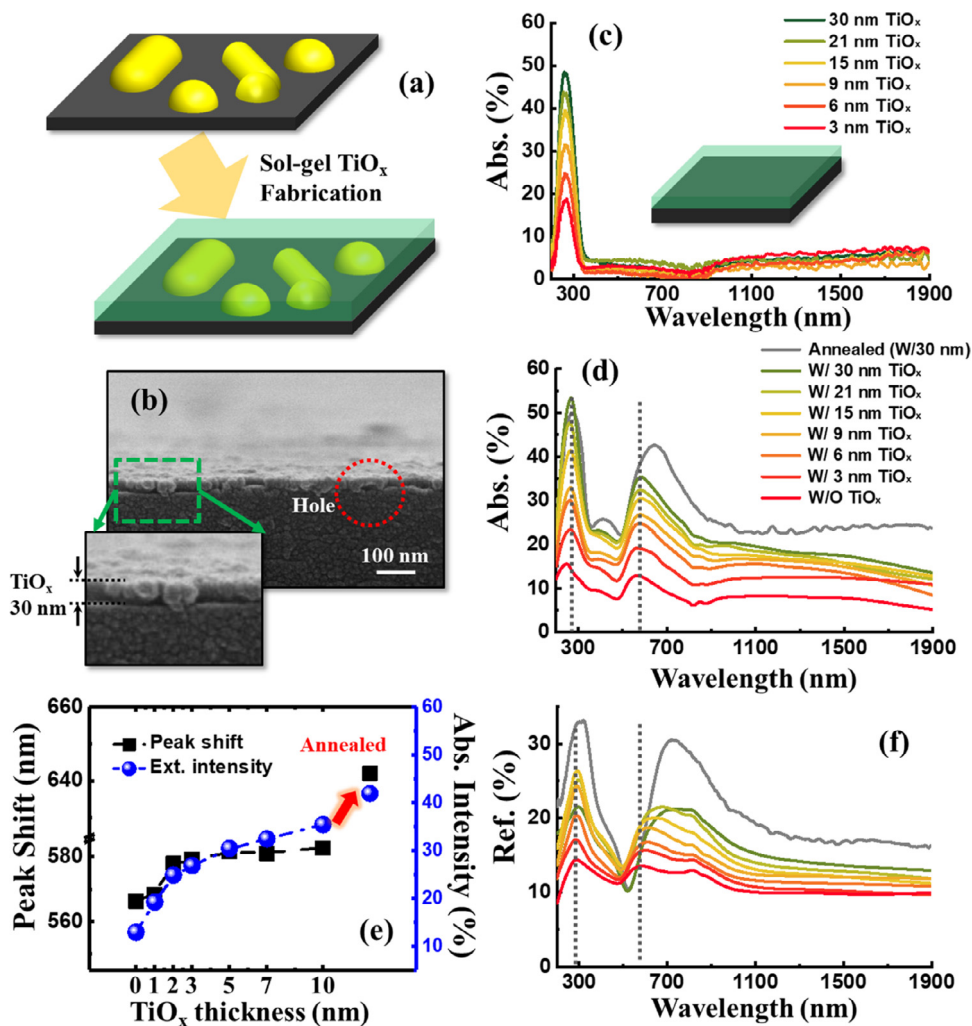


**Fig. 6.** Fabrication of TiO<sub>x</sub>/Au network hybrid film. (a) Diagram of hybrid thin-film fabrication. (b) Cross-sectional SEM image of TiO<sub>x</sub>/Au network hybrid film. (c) Absorption spectra of pure TiO<sub>x</sub> along coating thickness. (d) Absorption spectra of the TiO<sub>x</sub>/Au network hybrid films, and (e) absorption peak shift and intensity evolution plotted versa TiO<sub>x</sub> thickness. (f) Reflectance spectra of the TiO<sub>x</sub>/Au network hybrid films.

comparison with absorption due to the plasmon decay induced light re-emission [39].

### 3.4. Enhanced optoelectronic performance of $\text{TiO}_x$ through Au LSPR

With the sputtering of Al electrodes, the hybrid film was fabricated as a simple photodetector for solar irradiation detection. Distinguished by previous SERS spectra, Au network film exhibited a weaker plasmonic effect with the monochromatic excitation of 532 nm. However, the situation can be reversed as the solar irradiation is polychromatic light source over UV–VIS–IR. Seen in Fig. 7(a), although hybrid film of Au network showed a little bit weaker absorption between 500 and 700 nm in comparison to HS-NP hybrid film, a more consistent absorption was observed between hybrid film of Au network and solar irradiation spectrum in the overall range. The photocurrent characterization was performed within the voltage range between  $\pm 8$  V. Since the solar irradiation contains 7% of UV components [40], pure  $\text{TiO}_x$  film showed a photocurrent of  $9.0 \times 10^{-8}$  A with an ON/OFF ratio of  $\sim 60$  as seen in Fig. 7(b) and (c). Meanwhile, both HS-NP and network hybrid film showed obvious enhancement as plasmon triggered by light shining can significantly restrain the electron/hole recombination at near field areas [41,42]. Therefore, huge magnification on photocurrent was observed for

both samples as shown in Fig. 7(b), (c-1) and (c-2). In specific, the photocurrent of HS-NP and network hybrid film was enhanced to  $5.6 \times 10^{-7}$  and  $1.2 \times 10^{-6}$  A respectively with the ON/OFF ratio promotion to 538 and 907. The characterization matches well with the expectation from absorption and analysis displayed previously, as the photocurrent showed a significant increase by nearly twice owing to the enhanced LSPR in NIR region.

The photocurrent-time (I-T) cycle test was performed under 8 V and the result is plotted in Fig. 7(d). As seen, within the cycling duration, the performance of both hybrid film are stable in terms of maximum photocurrent. For a single cycling duration, it took  $\sim 220$  and  $\sim 330$  s for Au network and HS-NPs case, respectively. In specific, the photocurrent took 31 s to reach 80% of maximum in Au network case and the comparable duration of 33 s was observed for HS-NP case. However, in terms of the decay speed, network showed a rapid decay within 16 s to reach 20% maximum, while 4-time longer duration was observed for HS-NPs as 65 s. The response of photo detection is evaluated by photo-responsivity ( $R_p$ ) expressed as  $R_p = I_{on} - I_{off} / P\sigma$ , where  $P$  and  $\sigma$  are illumination power and effective illumination area, respectively. In our case, the  $\sigma$  between electrodes is  $0.15 \times 4 \text{ mm}^2$  and  $P$  is  $100 \text{ mW/cm}^2$ . The calculated  $R_p$  was plotted in Fig. 7(e) and as seen, the  $R_p$  of  $\text{TiO}_x$  was  $0.16 \text{ mA/W}$  with the polychromatic light excitation of solar simulator. With the enhancement

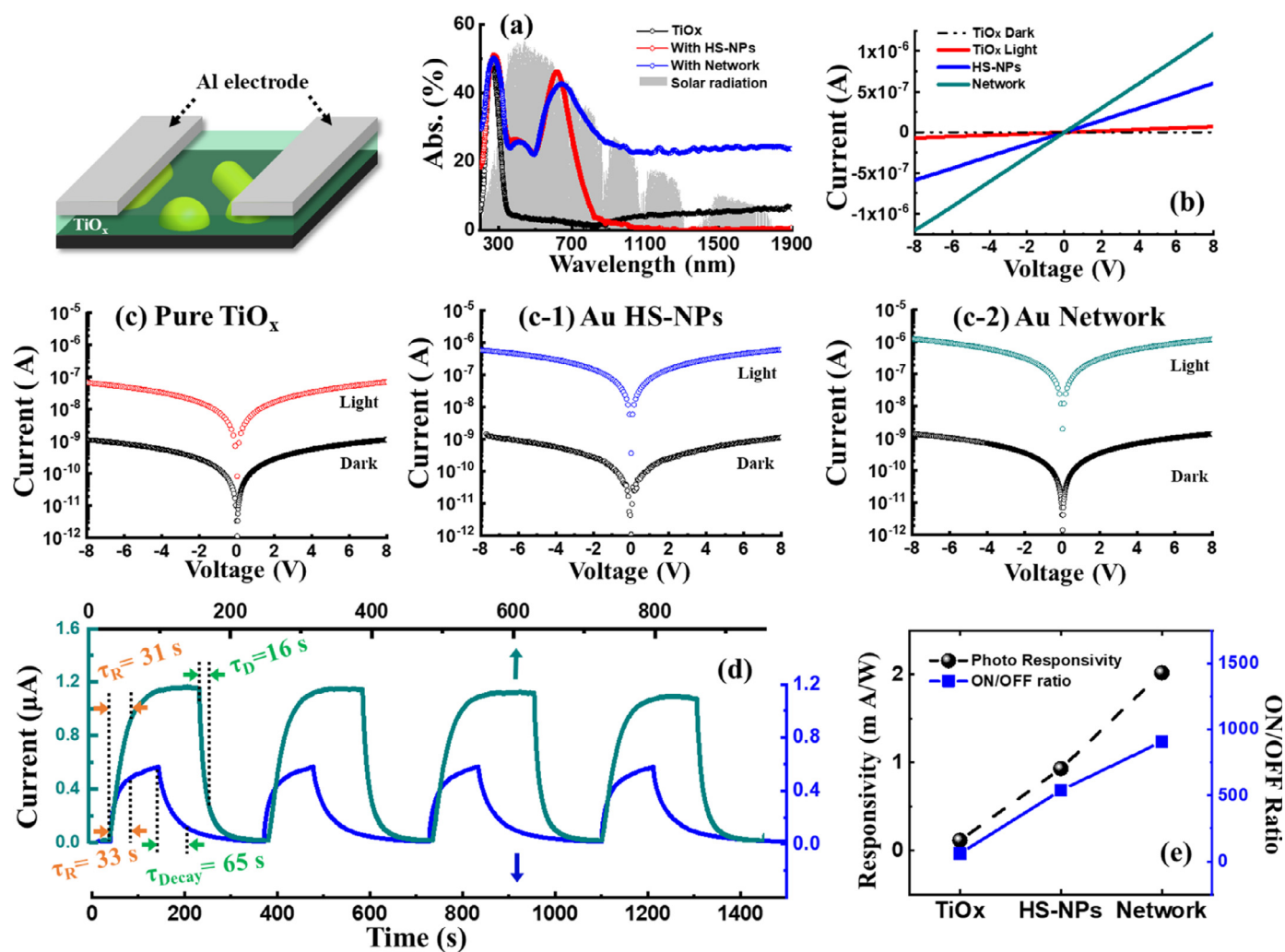


**Fig. 7.** Photoelectric characterization for  $\text{TiO}_x$ ,  $\text{TiO}_x/\text{HS-NP}$  and  $\text{TiO}_x/\text{Au Network}$  hybrid films. (a) Spectral comparison between solar irradiation and film absorption. (b) Photocurrent responds of  $\text{TiO}_x$ ,  $\text{TiO}_x/\text{HS-NP}$  and  $\text{TiO}_x/\text{Au Network}$  hybrid films versus drive voltage. (c) Photocurrent responds of pure  $\text{TiO}_x$  between  $\pm 8$  V plotted in logarithmic coordinates and the corresponding plots for  $\text{TiO}_x/\text{HS-NP}$  and  $\text{TiO}_x/\text{Au network}$  hybrid films are shown in (c-1)–(c-2). (d) Current-time cycling test for  $\text{TiO}_x/\text{HS-NP}$  and  $\text{TiO}_x/\text{Au network}$  hybrid films under 8 V. (e) Summary of photo-responsivity and ON/OFF ratio for each sample.

of Au HS-NPs and network, the  $R_p$  was significantly increased to 0.93 and 2.02 mA/W by 5.8 and 12.6 times.

#### 4. Conclusions

In this work, the Au network NSs were fabricated via SSD from the originally deposited Au film on quartz substrate. By variation of annealing time and temperature, morphological evolution from Au continuous film to network and isolated HS-NPs were successfully demonstrated with the control through surface diffusion length and surface energy minimization mechanism. Consisting of the mixture of irregular NSs that formed with relatively random configuration, the Au network exhibited an extremely widened LSPR absorption between 500 and 1900 nm in comparison with the common Au NSs, such as sphere and rods. The optical properties of Au individual NSs are correspondingly analyzed by FDTD method in terms of E-field distribution and extinction efficiency. It is found that the irregular NSs possess strong dipolar near E-field and even 3-time higher extinction efficiency than HS-NPs when light-excited and thus would be potentially suitable for VIS-IR photo-electronic applications. The monochromatic LSPR properties of corresponding samples were characterized via SERS for R6G molecular by 532 nm laser excitation, in which the HS-NPs showed a larger enhancement than Au network as the HS-NPs possess higher visible absorption. However, with polychromatic light, e.g. solar simulator, a twice higher photocurrent value was observed for the  $TiO_x$  / Au network hybrid film since the wider LSPR absorption of Au network can lead to more efficient utilization of polychromatic light energy.

#### Declaration of Competing Interest

The authors declare that they have no known competing financial interests or personal relationships that could have appeared to influence the work reported in this paper.

#### Acknowledgements

This work was supported by the National Natural Science Foundation of China (Grant Nos. 51473082, 51703104), the China Postdoctoral Science Foundation (Grant No. 2018M640613), the Program of Introducing Talents of Discipline to Universities (“111” plan), State Key Project of International Cooperation Research (Grant No. 2016YFE0110800), the 1st Level Discipline Program of Shandong Province of China, Qingdao Municipal Applied Basic Research Programs (Grant No. 182219jch). Financial support in part from the National Research Foundation of Korea (no. NRF-2019R1A2C4069438 and NRF-2018R1A6A1A03025242) (for Jihoon Lee) is gratefully acknowledged.

#### Supplementary materials

Supplementary material associated with this article can be found in the online version at doi:10.1016/j.actamat.2020.02.050.

#### References

- [1] T. Liu, Lucas V. Besteiro, Z. Wang, A.O. Govorov, Generation of hot electrons in nanostructures incorporating conventional and unconventional plasmonic materials, *Faraday Discuss* 214 (0) (2019) 199–213.
- [2] B.-Q. Chen, C. Zhang, J. Li, Z.-Y. Li, Y. Xia, On the critical role of Rayleigh scattering in single-molecule surface-enhanced Raman scattering via a plasmonic nanogap, *Nanoscale* 8 (34) (2016) 15730–15736.
- [3] D. Su, S. Jiang, M. Yu, G. Zhang, H. Liu, M.-Y. Li, Facile fabrication of configuration controllable self-assembled Al nanostructures as UV SERS substrates, *Nanoscale* (2018).
- [4] S. Yue, F. Lin, Q. Zhang, N. Epie, S. Dong, X. Shan, D. Liu, W.-K. Chu, Z. Wang, J. Bao, Gold-implanted plasmonic quartz plate as a launch pad for laser-driven photoacoustic microfluidic pumps, in: *Proceedings of the National Academy of Sciences*, 116, 2019, p. 6580.
- [5] Y. Li, J.G. DiStefano, A.A. Murthy, J.D. Cain, E.D. Hanson, Q. Li, F.C. Castro, X. Chen, V.P. Dravid, Superior plasmonic photodetectors based on Au@mos2 core-shell heterostructures, *ACS Nano* 11 (10) (2017) 10321–10329.
- [6] L. Li, H. Ruan, C. Liu, Y. Li, Y. Shuang, A. Alù, C.-W. Qiu, T.J. Cui, Machine-learning reprogrammable metasurface imager, *Nat. Commun.* 10 (1) (2019) 1082.
- [7] L. Shao, X. Zhuo, J. Wang, Advanced plasmonic materials for dynamic color display, *Adv. Mater.* 30 (16) (2018) 1704338.
- [8] R. Chikkaraddy, B. de Nijs, F. Benz, S.J. Barrow, O.A. Scherman, E. Rosta, A. Demetriadou, P. Fox, O. Hess, J.J. Baumberg, Single-molecule strong coupling at room temperature in plasmonic nanocavities, *Nature* 535 (2016) 127.
- [9] S. Mao, J. Liu, Y. Pan, J. Lee, Z. Yao, P. Pandey, S. Kunwar, Z. Zhu, W. Shen, L.A. Belfiore, J. Tang, Morphological and optical evolution of metallic oxide/Au nanoparticle hybrid thin film: high absorption and reflectance by plasmonic enhancement, *Appl. Surf. Sci.* 495 (2019) 143575.
- [10] P.R. West, S. Ishii, G.V. Naik, N.K. Emani, V.M. Shalae, A. Boltasseva, Searching for better plasmonic materials, *Laser Photon Rev.* 4 (6) (2010) 795–808.
- [11] C. Leng, X. Zhang, F. Xu, Y. Yuan, H. Pei, Z. Sun, L. Li, Z. Bao, Engineering gold nanorod-copper sulfide heterostructures with enhanced photothermal conversion efficiency and photostability, *Small* 14 (12) (2018) 1703077.
- [12] T. Chung, Y. Lee, M.-S. Ahn, W. Lee, S.-I. Bae, C.S.H. Hwang, K.-H. Jeong, Nanoislands as plasmonic materials, *Nanoscale* 11 (18) (2019) 8651–8664.
- [13] N. Bhalla, A. Jain, Y. Lee, A.Q. Shen, D. Lee, Dewetting metal nanofilms—effect of substrate on refractive index sensitivity of nanoplasmonic gold, *Nanomaterials* 9 (11) (2019) 1530.
- [14] Y. Gu, L. Zhang, J.K.W. Yang, S.P. Yeo, C.-W. Qiu, Color generation via subwavelength plasmonic nanostructures, *Nanoscale* 7 (15) (2015) 6409–6419.
- [15] N. Bhalla, S. Sathish, C.J. Galvin, R.A. Campbell, A. Sinha, A.Q. Shen, Plasma-Assisted large-scale nanoassembly of metal-insulator bioplasmonic mushrooms, *ACS Appl. Mater. Interf.* 10 (1) (2018) 219–226.
- [16] V.K. Pustovalov, L.G. Astafyeva, W. Fritzsche, Analysis of optical properties of spherical metallic nanoparticles for effective absorption of solar radiation and their heating, *Solar Energy* 122 (2015) 1334–1341.
- [17] F. Ruffino, M.G. Grimaldi, Controlled dewetting as fabrication and patterning strategy for metal nanostructures, *phys. status sol.* 212 (8) (2015) 1662–1684.
- [18] M. Kang, S.-G. Park, K.-H. Jeong, Repeated solid-state dewetting of thin gold films for nanogap-rich plasmonic nanoislands, *Sci Rep.* 5 (1) (2015) 14790.
- [19] L. Gao, F. Lemarchand, M. Lequime, Comparison of different dispersion models for single layer optical thin film index determination, *Thin Sol. Films* 520 (1) (2011) 501–509.
- [20] S. Sarkar, V. Gupta, M. Kumar, J. Schubert, P.T. Probst, J. Joseph, T.A.F. König, Hybridized guided-mode resonances via colloidal plasmonic self-assembled grating, *ACS Appl. Mater. Interf.* 11 (14) (2019) 13752–13760.
- [21] H.R. Philipp, - Silicon Dioxide (SiO<sub>2</sub>) (Glass), in: E.D. Palik (Ed.), *Handbook of Optical Constants of Solids*, Academic Press, Burlington, 1997, pp. 749–763.
- [22] C.V. Thompson, Solid-State dewetting of thin films, *Annu. Rev. Mater. Res.* 42 (1) (2012) 399–434.
- [23] J. Basu, C.B. Carter, R. Divakar, B. Mukherjee, N. Ravishankar, Nanopatterning by solid-state dewetting on reconstructed ceramic surfaces, *Appl. Phys. Lett.* 94 (17) (2009) 171114.
- [24] P.R. Gadkari, A.P. Warren, R.M. Todi, R.V. Petrova, K.R. Coffey, Comparison of the agglomeration behavior of thin metallic films on SiO<sub>2</sub>, *J. Vac. Sci. Technol. A* 23 (4) (2005) 1152–1161.
- [25] F. Ruffino, A. Pugliara, E. Carria, L. Romano, C. Bongiorno, G. Fiscaro, A. La Magna, C. Spinella, M.G. Grimaldi, Towards a laser fluence dependent nanostructuring of thin Au films on Si by nanosecond laser irradiation, *Appl. Surf. Sci.* 258 (23) (2012) 9128–9137.
- [26] M. Hövel, B. Gompf, M. Dressel, Dielectric properties of ultrathin metal films around the percolation threshold, *Phys. Rev. B* 81 (3) (2010) 035402.
- [27] S.S. Mirshafieyan, T.S. Luk, J. Guo, Zeroth order Fabry-Perot resonance enabled ultra-thin perfect light absorber using percolation aluminum and silicon nanofilms, *Opt. Mater. Expr.* 6 (4) (2016) 1032–1042.
- [28] M. Sui, P. Pandey, M.-Y. Li, Q. Zhang, S. Kunwar, J. Lee, Tuning the configuration of Au nanostructures: from vermiform-like, rod-like, triangular, hexagonal, to polyhedral nanostructures on c-plane GaN, *J. Mater. Sci.* 52 (1) (2016) 391–407.
- [29] E. Jiran, C.V. Thompson, Capillary instabilities in thin, continuous films, *Thin Sol. Films* 208 (1) (1992) 23–28.
- [30] F. Ruffino, A. Canino, M.G. Grimaldi, F. Giannazzo, F. Roccaforte, V. Raineri, Kinetic mechanism of the thermal-induced self-organization of Au/Si nanodroplets on Si (100): size and roughness evolution, *J. Appl. Phys.* 104 (2) (2008) 024310.
- [31] M. Sui, P. Pandey, M.-Y. Li, Q. Zhang, S. Kunwar, J. Lee, Tuning the configuration of Au nanostructures: from vermiform-like, rod-like, triangular, hexagonal, to polyhedral nanostructures on c-plane GaN, *J. Mater. Sci.* 52 (1) (2017) 391–407.
- [32] H. Krishna, C. Favazza, A.K. Gangopadhyay, R. Kalyanaraman, Functional nanostructures through nanosecond laser dewetting of thin metal films, *JOM* 60 (9) (2008) 37–42.
- [33] V.I. Kukushkin, A.B. Van'kov, I.V. Kukushkin, Long-range manifestation of surface-enhanced Raman scattering, *JETP Lett.* 98 (2) (2013) 64–69.
- [34] W. Chen, S. Zhang, M. Kang, W. Liu, Z. Ou, Y. Li, Y. Zhang, Z. Guan, H. Xu, Probing the limits of plasmonic enhancement using a two-dimensional atomic crystal probe, *Light: Sci. Appl.* 7 (1) (2018) 56.
- [35] E.C. Le Ru, P.G. Etchegoin, Chapter 5 - Calculations of electromagnetic enhancements, in: E.C. Le Ru, P.G. Etchegoin (Eds.), *Principles of Surface-Enhanced Raman Spectroscopy*, Elsevier, Amsterdam, 2009, pp. 265–297.
- [36] P.K. Jain, K.S. Lee, I.H. El-Sayed, M.A. El-Sayed, Calculated absorption and scattering properties of gold nanoparticles of different size, shape, and composition: applications in biological imaging and biomedicine, *J. Phys. Chem. B* 110 (14) (2006) 7238–7248.

- [37] H. Chen, L. Shao, K.C. Woo, T. Ming, H.-Q. Lin, J. Wang, Shape-Dependent refractive index sensitivities of gold nanocrystals with the same plasmon resonance wavelength, *J. Phys. Chem. C* 113 (41) (2009) 17691–17697.
- [38] T.R. Jensen, M.L. Duval, K.L. Kelly, A.A. Lazarides, G.C. Schatz, R.P. Van Duyne, Nanosphere lithography: effect of the external dielectric medium on the surface plasmon resonance spectrum of a periodic array of silver nanoparticles, *J. Phys. Chem. B* 103 (45) (1999) 9846–9853.
- [39] C. Clavero, Plasmon-induced hot-electron generation at nanoparticle/metal-oxide interfaces for photovoltaic and photocatalytic devices, *Nat. Photon.* 8 (2014) 95–103.
- [40] C.A. Gueymard, Parameterized transmittance model for direct beam and circum-solar spectral irradiance, *Solar Energy* 71 (5) (2001) 325–346.
- [41] A. Furube, S. Hashimoto, Insight into plasmonic hot-electron transfer and plasmon molecular drive: new dimensions in energy conversion and nanofabrication, *NPG Asia Mater.* 9 (12) (2017) e454–e454.
- [42] F. Tan, T. Li, N. Wang, S.K. Lai, C.C. Tsoi, W. Yu, X. Zhang, Rough gold films as broadband absorbers for plasmonic enhancement of TiO<sub>2</sub> photocurrent over 400–800 nm, *Sci Rep.* 6 (2016) 33049.